New diffraction directivity prestack attributes for seismic fracture prediction

Konstantin Smirnov[1*], Evgeny Landa[1] and Igor Fedyaev[1].

Abstract

Locating small-scale faults and fractures is an important task in reservoir characterization. These linear subsurface features generate azimuthally oriented diffractions. A diffraction directivity can be utilized for seismic fracture prediction. A numerical procedure was developed to calculate two new prestack diffraction attributes: the fracture azimuth and the fracture detection reliability. The new attributes can be used to refine structural and stratigraphic interpretation and to guide the fracture properties modelling in 3D geostatistical applications. The evaluation of these attributes on a field dataset containing a fractured reservoir showed promising results for seismic fracture characterization.

Introduction

Locating small-scale subtle subsurface features, including faults and fractures, and determining their relative density and orientation in potential reservoirs is an important task in reservoir characterization. Various methods have been developed for identifying and mapping fractures. The extraction of fracture density and orientation from migrated 3D seismic volumes after the stack is probably one of the most popular techniques used. Diffraction imaging is an alternative method for detecting and mapping faults and fractures (Khaidukov et al., 2004; Landa, 2012; Tyiasning et al., 2016). Diffraction imaging uses direct responses of small-scale subsurface geologic features in the prestack domain, while traditional seismic attributes such as incoherence and curvature are computed in the final images. The integration of diffraction imaging results with standard seismic attributes can significantly refine structural and stratigraphic interpretation. Diffraction data can also be used as external trends to propagate fracture properties in the inter-well space, to create more reliable models of fractured reservoirs.

The most common result of 3D diffraction imaging is a diffraction cube. Based on this cube, one can evaluate diffraction intensity, diffraction energy, and other diffraction post-imaging attributes. Diffraction images can also be used for spectral decomposition to increase confidence in small-scale geological feature detection. The diffraction image, its attributes, and the attributes calculated from the migrated images, such as coherence, minimum, and maximum curvature, which are widely used in the interpretation and characterization of the reservoir, can have limited reliability due to the inaccuracies and uncertainties introduced when constructing these images. When dealing with point-like objects such as karsts, small voids, or sinkholes, diffraction propagates radially and isotopically in all directions. Diffraction imaging, in this case, focuses propagated diffraction energy back onto the objects and they are well imaged. In a more specific case, when the goal is to detect linear elements of the Earth's interior, such as fault planes and fractures, diffraction imaging using point diffractor operators can be non-optimal. A more efficient algorithm can be developed using edge diffraction. Unlike a point diffractor, an edge diffractor forms conical wave-fronts from each point of the lineament (Keller, 1962; Klem-Musatov, 1980). As a result, only traces that intersect with the edge diffraction cone contain the diffraction response from a certain point of the linear diffractor.

Thus, the analysis of the diffraction component of the total wavefield on the original prestack data allows for the prediction of the orientation of linear diffractors (fractures). In this case, the geophysicist will have additional seismic attributes specifically designed to characterize the fractures, including their orientation.

In this paper, we present two new attributes computed from the diffractivity component of the total wavefield. The first attribute is the fracture azimuth, and the second is the fracture detection reliability factor. The evaluation of these attributes on a real dataset shows promising results for fracture prediction.

The point and the line diffractions

We distinguish two types of diffraction: (1) point or tip diffraction from isolated scatterers or small-scale heterogeneities such as circular reefs or karsts, and (2) edge diffraction from linear diffractors such as edges or terminations of continuous reflectors, fault planes, and fracture zones. When the incident wave hits

[1] PetroTrace Geoscience

[*] Corresponding author, E-mail: konstantin.smirnov@ptgeos.com

DOI: 10.3997/1365-2397.fb2021010

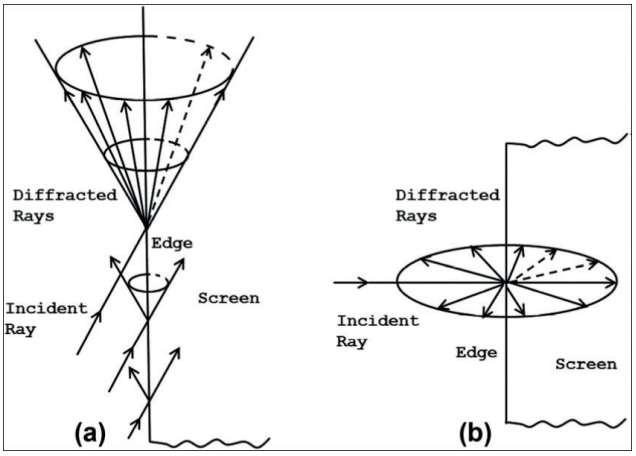

Figure 1 The cone of diffracted rays produced by an incident ray which hits the edge (a) obliquely to the edge and (b) normal to the edge (Keller, 1962).

a corner or a point-like object, diffraction propagates radially and isotropically in all directions, and when the incident ray hits an edge or fracture, it is diffracted in a more complex manner (Figure 1).

According to the geometric theory of diffraction (GTD) (Keller, 1962; Klem-Musatov, 1980), if the incident wave propagates in a direction oblique to the edge, each point of the diffractor creates an edge diffraction wave with a conical wavefront when the edge is the axis of the cone (see Figure 1, right). Only certain traces of the observed data register the edge diffraction from a specified point of the linear diffractor. These traces are defined by the spatial position of the shot, diffraction point, and azimuth of the linear diffractor.

The migrated dip-azimuth angle domain is very convenient to work with diffractions. The principles of computing common image gather in the migrated dip-azimuth angle domain are well established (Audebert et al., 2002; Koren and Ravve, 2005). Reflection events in this domain have a concave shape and can be described by an analytical 'smile' like surface with a stationary point regardless of the migration velocity used; a diffraction is flat in this domain. This significant difference in reflection and diffraction shapes allows the development of efficient algorithms for their separation (Reshef and Landa, 2009).

Figure 2 shows the models of the point and line scattering objects, and their diffraction responses on the depth slices of synthetic azimuthal dip-angle gathers. As predicted by theory, a point diffractor is represented by an azimuthally isotropic flat circle, and a linear diffractor is an ellipse with a long axis perpendicular to the diffractor (Klokov et al., 2011, Landa, 2012, Dell et al., 2019a, 2019b).

One way to estimate fracture orientation is to compute dip-angle gathers for different azimuthal sectors after reflection suppression. The resulting stacked dip-angle gathers can be used to select the flattest one associated with the correct azimuth of the lineament (Klokov et al., 2011). While this approach is

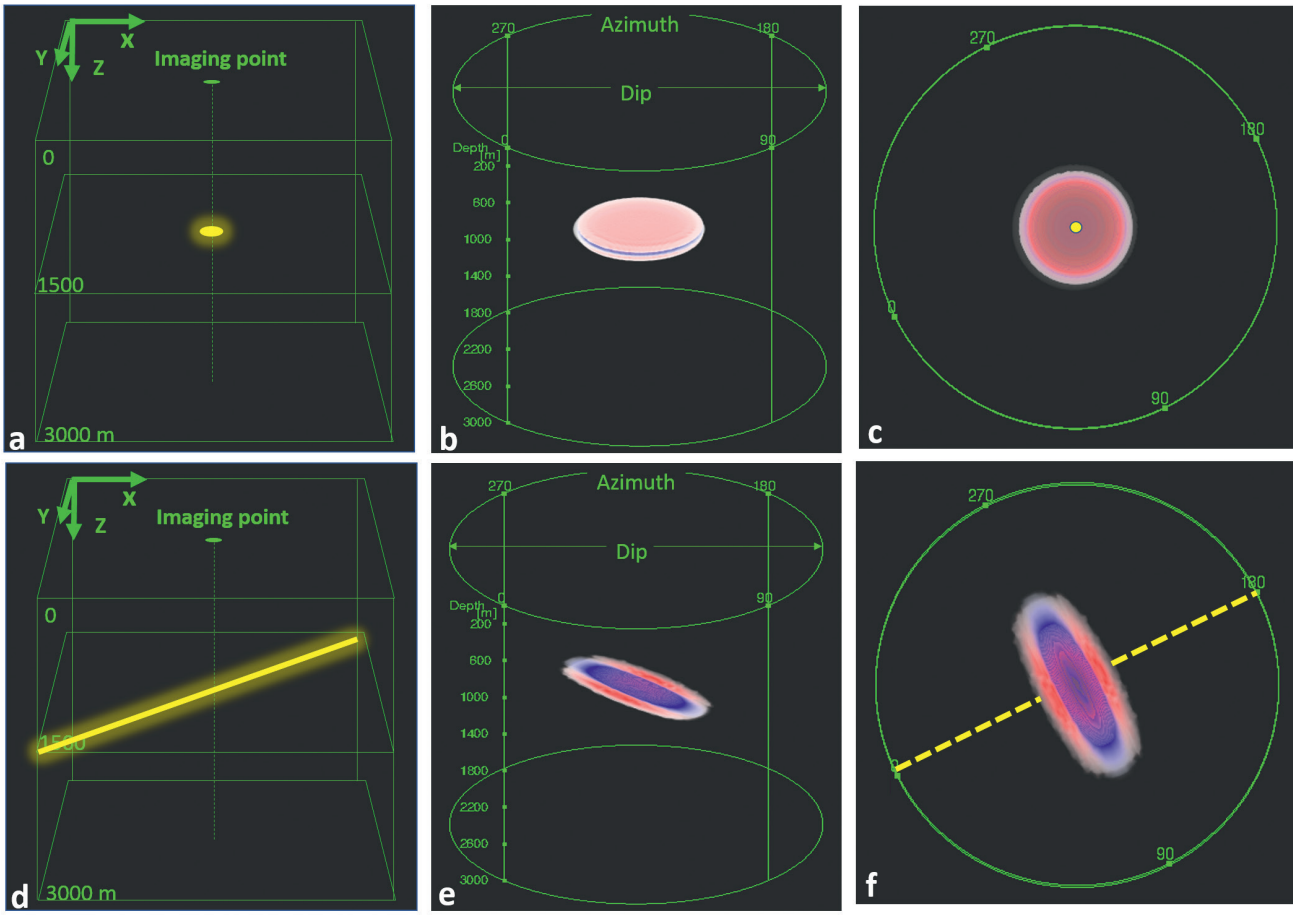

Figure 2 (a) The point scattering object, (b) its diffraction image on the dip-angle gather, and (c) top view of the dip-angle gather. (d) The linear scattering object, (e) its diffraction image on the dip-angle gather, and (f) top view of the dip-angle gather. The image point indicates the dip-angle gather location.

not difficult to implement, it has several disadvantages. First, the choice of the size and number of azimuth sectors will be subjective, and second, the calculation and analysis of several gather datasets can take quite a long time. Therefore, instead of dealing with multiple gathers for different azimuthal sectors, we decided to evaluate the directivity of the diffractors directly on the full azimuthal gather.

The method

An ellipse with the major axis A and the minor axis B can approximate the edge diffraction shape on the dip-azimuth angle gathers (Figure 3). If the elongation of the ellipse (A/B ratio) is close to one (a circle), then the diffraction response is azimuthally independent and most likely caused by a point-like diffractor (e.g., reef or karts). If the A/B ratio is larger than one, then the diffraction response is azimuthally oriented in 3D space and most likely induced by a fault or fracture. The B axis of the ellipse indicates the fault/fracture orientation.

A numerical procedure was developed to calculate the diffraction ellipse and estimate the A and B axes. The input data for the calculation are dip-azimuth gathers after reflection suppression. For each depth point, the procedure calculates the diffraction energy as a function of the A and B axis lengths and azimuth. First, we scan the azimuths to find the main diffraction orientation and then calculate the optimal lengths for A and B. To minimize the computation time, the user can control the azimuth step, depth step, and other parameters.

For each imaging point and for each dip-azimuth gather location, the described procedure calculates two new diffraction attributes: 1) the relationship between the A and B axes of the ellipse (A/B ratio) and 2) The azimuth of the small axis B. These attributes form an A/B ratio and B-azimuth cubes. The cube with azimuth B defines the fracture orientation, and the A/B cube can be considered as the reliability of the fracture detection. The larger the A/B value, the more confidently one can say that an elongated diffractor or a fracture causes the diffraction energy. These new diffraction attributes can be used to analyse data along target horizons and to generate fracture vector maps.

Real data example

We applied the new diffraction attribute technology to a field dataset imaging a fractured reservoir. The average depth of the Devonian carbonate reservoir is 2500 m with a reservoir thickness of up to 38 m. There is a complicated fault network with fractures connecting different void types and therefore increasing fluid flow and the reservoir permeability. Figure 4 shows the reservoir top horizon map and the fracture information estimated in wells. Based on the well information, it can be concluded that, although fractures have different orientations, the average maximum horizontal stress azimuth is NW-SE. The fracture density information was not available.

The original seismic data were processed using a time processing workflow. A detailed velocity model was built for depth imaging. The velocity model and the processed gathers were the input for the prestack depth migration and computation of conventional reflection angle gathers and dip angle gathers. The

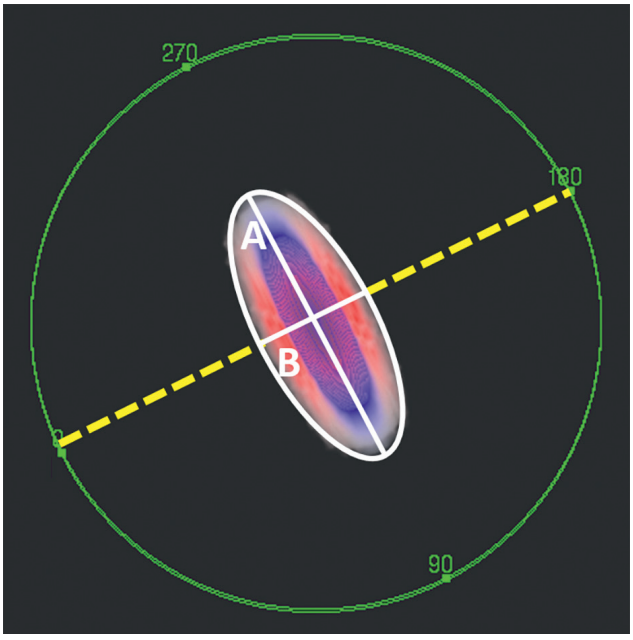

Figure 3 The diffraction approximated by an ellipse.

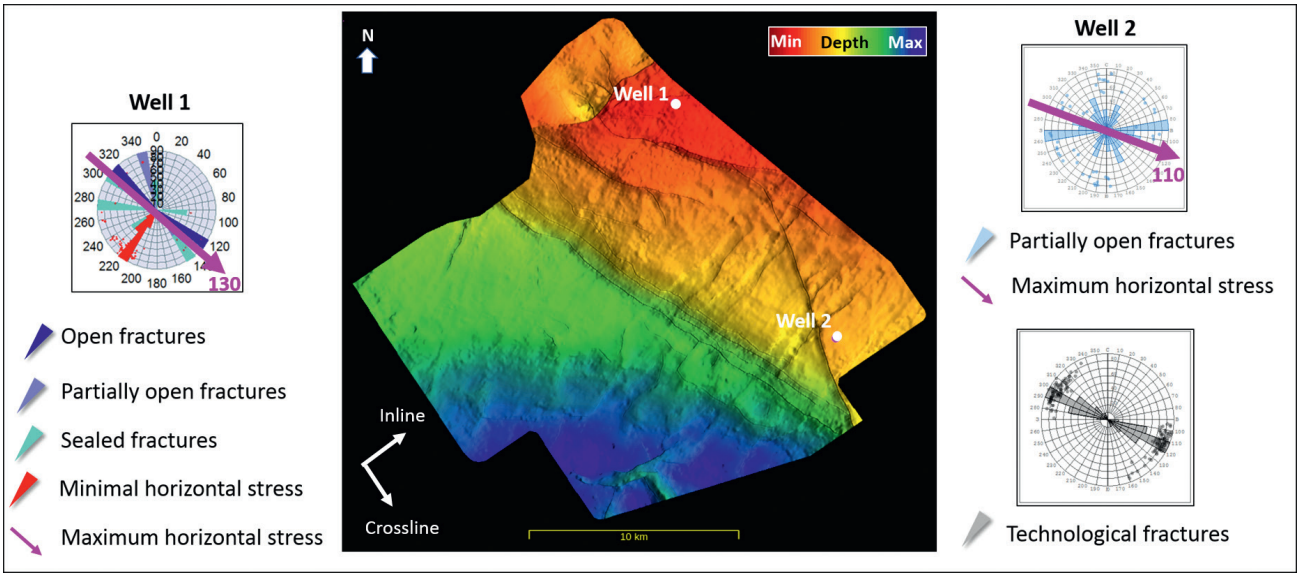

Figure 4 The target horizon depth and the well based fractures distribution.

migrated reflection angle gathers were used to create a standard specular reflection volume. The calculated volume was the input for the traditional coherence attribute generation. The obtained migrated dip angle gathers were processed by the 3D high-resolution Radon filter, to suppress specular reflections. After stacking the filtered gathers, a diffraction volume was generated. The 3D high-resolution Radon filter sufficiently removes specular reflections from the prestack data regardless of the structural dip. Therefore, the complex reservoir relief does not impact the diffraction imaging results. Figure 5 shows the coherency and diffraction images along the target horizon. The diffraction data confirm major subsurface discontinuities.

Figure 6 shows a zoomed in version of the coherency map in Figure 5 including well 1 to the north together with slices of dip-azimuth gathers at the fault and reef locations after reflection suppression.

As expected, the diffraction response from the reef is azimuthally independent, while the diffraction response from the fault is oriented perpendicular to the fault. The new attributes were calculated to predict reliability of fracture distribution and estimate fracture orientation. Figure 7 shows the fracture azimuth (B-azimuth attribute) and the fracture reliability (A/B attribute) along the target interval.

The new attributes can be utilized to create a fracture vector map where the vector orientation indicates a fracture azimuth at every point of the subsurface. The fracture vectors can be colour coded by the azimuth and by the fracture reliability. Figures 8-10 depict the enlarged

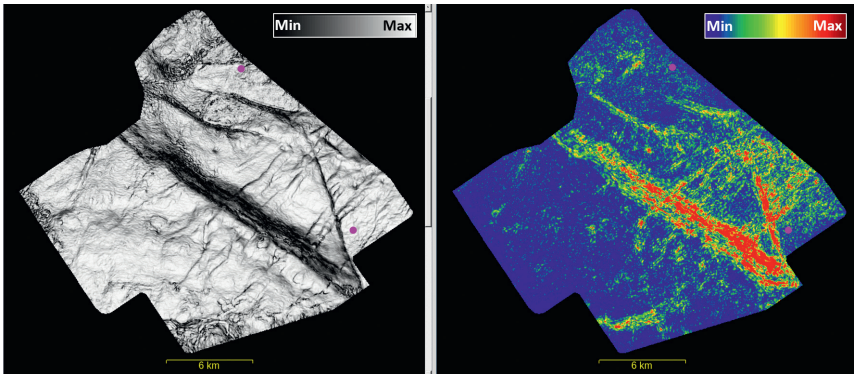

Figure 5 (left) The coherency and (right) diffraction image along the target horizon.

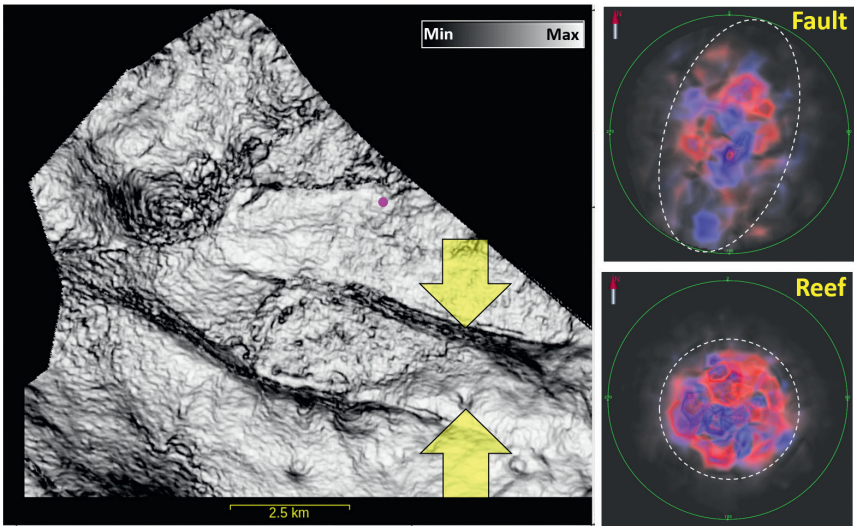

Figure 6 The coherency map of the northern part of the survey, diffraction from the fault and diffraction from the reef. The yellow arrows indicate the diffractions locations (upper is the fault, lower is the reef).

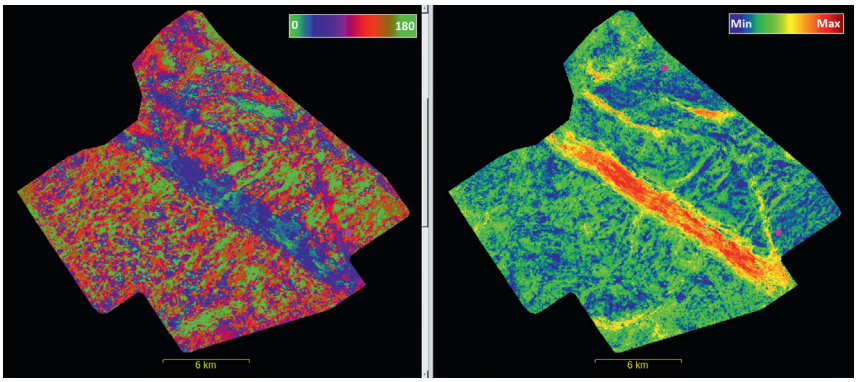

Figure 7 The new diffraction attributes in the target interval: (left) fracture azimuth and (right) fracture reliability.

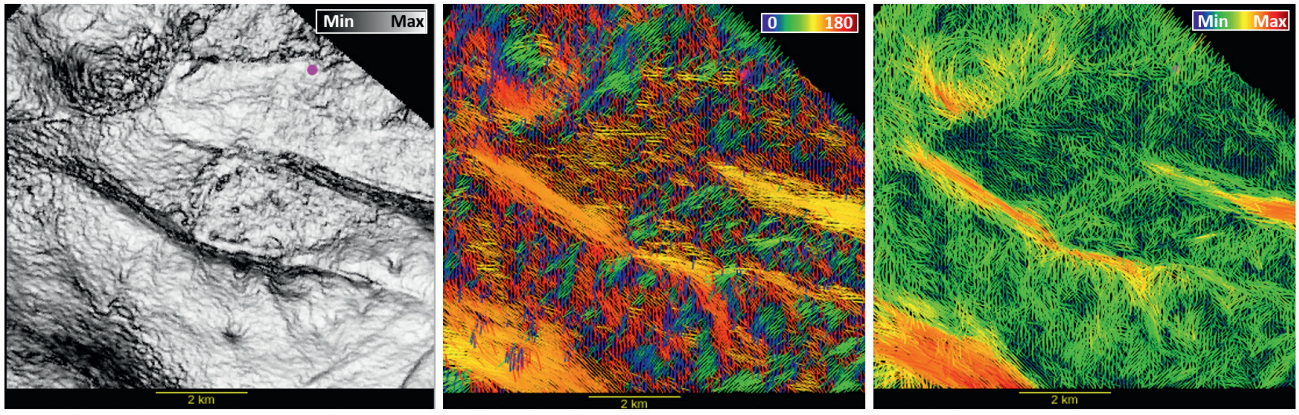

Figure 8 The attributes in the target interval for the northern part of the survey: (left) coherency, (centre) the fracture vectors coloured by the azimuth and (right) the fracture vectors coloured by the fracture reliability.

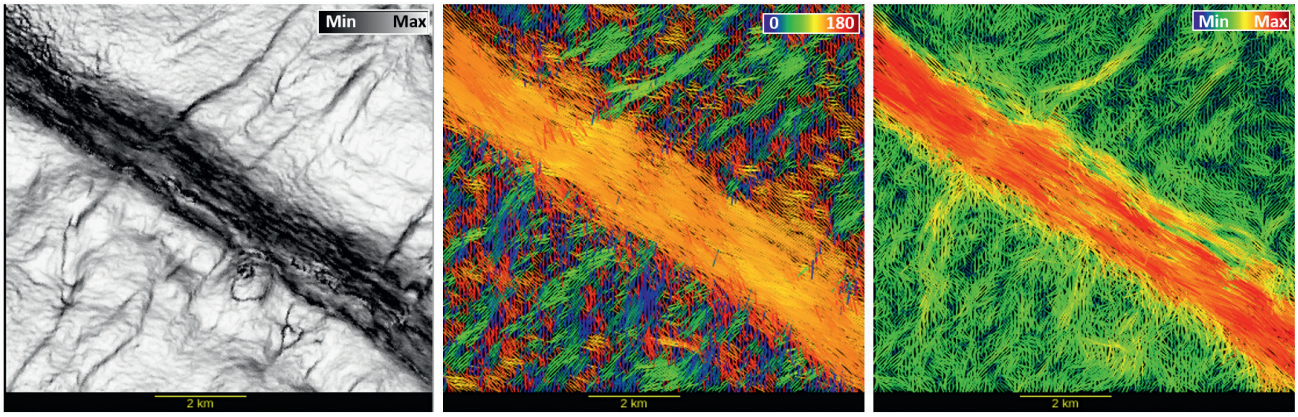

Figure 9 The attributes in the target interval for the central part of the survey: (left) coherency, (centre) the fracture vectors coloured by the azimuth and (right) the fracture vectors coloured by the fracture reliability.

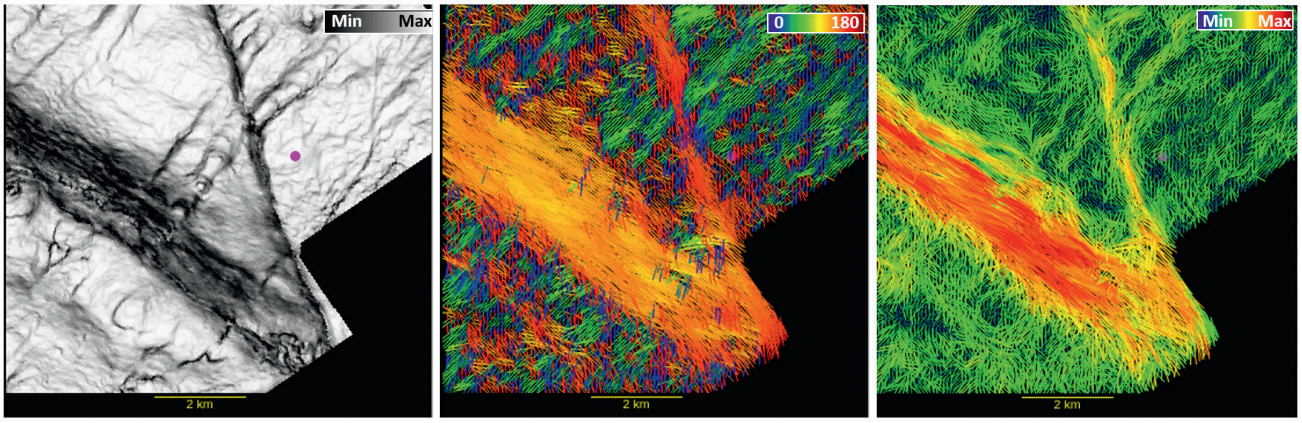

Figure 10 The attributes in the target interval for the southern part of the survey: (left) coherency, (centre) the fracture vectors coloured by the azimuth and (right) the fracture vectors coloured by the fracture reliability.

coherency and fracture vector maps for the different parts of the survey.

Results

It can be seen that the diffraction vectors are consistent with the main inhomogeneities in the coherence data. At the same time, some subtle geological features that may not be visible in traditional seismic attributes were discovered.

There is the NW-SE fault in the centre of the coherency in Figure 8. The calculated diffraction vectors indicate that the predicted fractures extend from this fault to the south forming a dovetail. This feature is especially prominent on the fracture azimuth map.

The large-scale NW-SE coherency anomaly in Figure 9 is most likely related to the area of the fracture development. The diffraction reliability shows that the fracture distribution is uneven in this area and the fracture density is probably higher in the northern part of this zone. One also cannot miss the second powerful discontinuity on the coherency in the NE-SW direction. The diffraction attributes show that before joining the large-scale

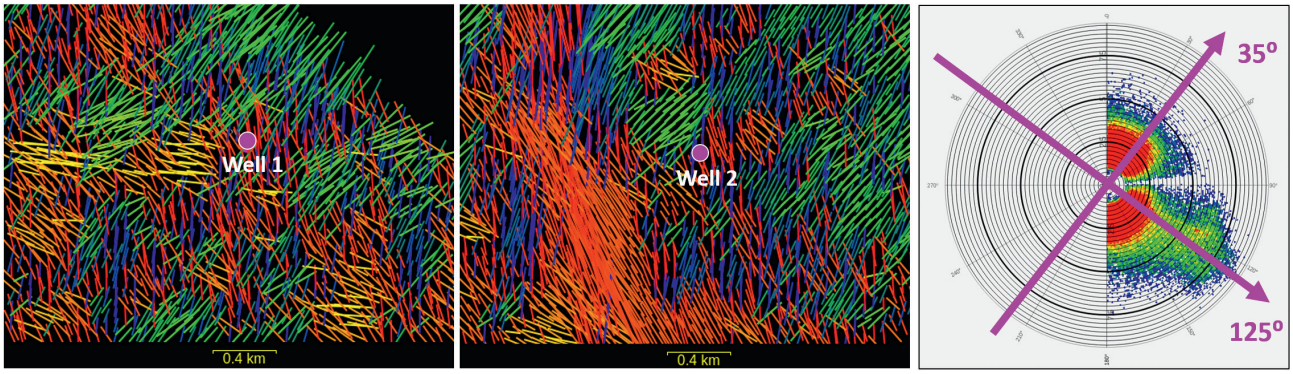

Figure 11 The diffraction vectors around the wells and the diffraction vectors rose diagram for the whole area.

NW-SE fracture corridor, this element splits apart producing the additional fracture lineament which is invisible on the coherency.

The diffraction attributes in Figure 10 confirm the major discontinuities but also indicate that the density of the predicted fractures vary along these lineaments. Figure 9 and Figure 10 also show that although the major diffractions orientation in the large fractured zone is NW-SE, some features with different azimuths can be found in this area.

It can be noticed that some discontinuities are not highlighted on the fracture reliability attribute. The probable reason is that we approximate a diffraction by an ellipse to calculate the fracture reliability. In reality, the shape of diffractions can be much more complicated.

Figure 11 shows the diffraction vectors around the wells and the diffraction vectors rose diagram for the whole area. According to the fracture distribution at well 1 (Figure 4), the fractures detected in the well have multiple azimuths. The diffraction vectors show that there is no apparent dominant fracture orientation at the well 1. Well 2 is located at the green cluster of diffraction vectors with the orientation matching the fracture azimuth detected in this well.

As expected, the diffraction vector rose diagram for the whole reservoir indicates two main orthogonal directions which correspond to the maximum and minimal stress azimuths estimated in the wells.

Conclusion

Diffraction imaging can detect reservoir-scale fault and fracture zones that may be difficult to detect in a conventional reflection image. In addition, analysis of the diffraction response on the dip-azimuth common image gathers distinguishes between point diffractors, such as small circular reefs or karsts, and elongated diffractive elements, such as fault planes or fractures. We have introduced two new diffraction attributes, namely the fracture azimuth and fracture detection confidence factor. An example of field data demonstrates the feasibility and effectiveness of the proposed method.

The authors would like to stress that the goal of the new diffraction attributes is not to replace conventional reflection attributes (coherence, curvature, etc.) but to extract additional information about small-scale subsurface discontinuities. The real data results showed that the diffraction attributes gave additional insight to the traditional coherence attribute. Since reflection and diffraction attributes are based on the same input data but produced by different technologies, these attributes complement each other to increase confidence in fracture characterization.

Discussion

The diffraction attributes presented are derived from wide-azimuth prestack data, suggesting that reliable results require the seismic survey to have regular sampling in offset and azimuth. A study on how a seismic survey design impacts the calculation results would be very useful to predict if the particular seismic dataset is suitable for the diffraction directivity prediction.

Another interesting topic to consider is what happens when multiple fractures of different azimuths intersect at the same subsurface location. We would propose detailed modelling of the diffraction response from multiple fractures and comparison of synthetics and real datasets.

In future projects with more well calibration points lies the challenge of multi-attribute integration and seismic/well data calibration. Seismic attribute integration can be performed by a probabilistic approach, a neural network technology or by other methods. Seismic/well calibration will always be challenging because of the different vertical resolution, but a robust calibration technique would provide the most valuable prediction from this fracture characterization workflow.

Acknowledgments

The authors thank NNK-SARATOVNEFTEGASDOBYCHA for permission to demonstrate the presented results. Special thanks also go to the PetroTrace processing and interpretation team for the support of this study.

References

Audebert, F., Froidevaux, P., Racotoarisoa, H. and Svay-Lucas, J. [2002]. Insights into migration in the angle domain. Expanded Abstract, SEG, 1188-1191.

Dell, S., Gajewski, D. and Hoelker, A. [2019]. Azimuthal Diffraction Imaging: a Land Data Example from Northern Switzerland, EAGE.

Dell, S., Hölker, A. and Gajewski, D. [2019]. Using seismic diffractions for assessment of tectonic overprint and fault interpretation. *Geophysics*, **84**(1), IM1-IM10.

Keller, J.B. [1962]. Geometrical Theory of Diffraction. *Journal of the Optical Society of America*, 1962, **52**(2), 116-130.

Khaidukov, V., Landa, E. and Moser, T.J. [2004]. Diffraction imaging by focusing-defocusing: An outlook on seismic superresolution: *Geophysics*, **69**(6), 1478-1490, http://dx.doi.org/10.1190/1.1836821.

Klem-Musatov, K.D. [1980]. Theory of Edge Waves and Application to Seismic, Nauka (in Russian), English translation: Theory of Seismic Diffraction, SEG, 1994.

Klokov, A., Baina, R. and Landa, E. [2011]. Point and Edge Diffractions in Three Dimensions, EAGE, Vienna.

Koren, Z. and Ravve, I. [2005]. Full-azimuth subsurface angle domain wavefield decomposition and imaging. Part I: directional and reflection image gathers. *Geophysics*, **76**(1), S1-S13.

Landa, E. [2012]. Seismic diffraction: where is the value? 82nd SEG Annual International Meeting, Expanded Abstracts, 1-4, doi: 10.1190/segam2012-1602.1.

Reshef, M. and E. Landa, E. [2009]. Post-stack velocity analysis in the dip-angle domain using diffractions. *Geophysical Prospecting*, **57**, 811-821, doi: 10.1111/j.1365-2478.2008.00773x.

Tyiasning, S., Merzlikin, D., Cooke, D. and Fomel, S. [2016]. A comparison of diffraction imaging to incoherence and curvature, *The Leading Edge*, 86-89.